RSC Sustainability

ROYAL SOCIETY OF CHEMISTRY

PAPER

View Article Online
View Journal | View Issue

Cite this: *RSC Sustainability*, 2025, **3**, 3049

Methane decomposition using a Ni–Cu-based hollow-wall-structured catalyst prepared by combined electroless plating†

Prithvi Rasaili, Ryo Watanabe,* Hiroshi Akama and Choji Fukuhara*

A bimetallic Ni–Cu catalyst, prepared using the electroless plating (ELP) method, demonstrated potential for catalytic methane decomposition (CMD) to produce turquoise hydrogen and carbon-capture materials. A structured catalyst was synthesised with a focus on optimising its design for enhanced activity, high-quality carbon capture, and improved resistance to early deactivation. Catalysts were characterised using FE-SEM, SEM-EDX, XRD, XRF, and Raman techniques. The 70–30 Ni–Cu catalyst was identified to be the best-performing catalyst; it exhibited a fine alloy structure, good performance, thermal stability, and high-temperature activity, and outperformed the corresponding impregnation-method-based catalyst. The Cu in the catalyst enhances the growth of filamentous carbon and improves the structural order of the carbon nanotubes (CNTs) owing to its carbon-dispersing effect and optimised active-site availability. However, excess Cu reduces the number of available active sites and decreases performance. The captured multiwalled CNTs in the best catalyst showed a higher I_G/I_D ratio (0.83) compared to commercial CNTs, which highlights their potential use in functional-material applications. The combination of a structured substrate and the ELP method has the potential to provide long-term turquoise H_2 production and carbon capture.

Received 27th March 2025
Accepted 13th May 2025

DOI: 10.1039/d5su00216h

rsc.li/rscsus

Sustainability spotlight

Our innovative research on methane decomposition supports United Nations Sustainable Development Goal (SDG) 7: Affordable and Clean Energy, using Electroless Plating (ELP) catalysts to convert methane—a potent greenhouse gas—into hydrogen (H_2) free of CO_x emissions, along with valuable carbon byproducts. This groundbreaking approach paves the way for sustainable clean hydrogen energy systems, addressing pressing challenges in emission reduction and energy accessibility. Furthermore, the solid carbon produced can be transformed into high-value functional materials with wide-ranging economic and technological applications. By enabling carbon-neutral hydrogen, significantly reducing methane emissions, and driving innovation in hydrogen technologies, this research contributes to building a cleaner, more sustainable, and equitable energy future while advancing SDG 7's vision of clean energy for all.

1 Introduction

Hydrogen is one of the most-promising clean energy sources owing to its high energy density and zero emission potential when used in fuel cells.[1,2] It can be produced from various feedstocks, including natural gas, biomass, coal, and water. Natural gas, which is primarily composed of methane, is the dominant source of hydrogen. Methane is abundantly available from both natural (*e.g.*, natural gas reserves) and artificial (*e.g.*, agricultural waste and biogas) sources.[3] However, conventional industrial methods for producing hydrogen, such as steam methane reforming (SMR) and the partial oxidation of methane (POM), are associated with significant CO_x (CO and CO_2) emissions. Despite integrating carbon-capture technologies, achieving net-zero emissions remains challenging due to the energy-intensive nature of the CO-conversion process and the need for additional hydrogen purification steps, which often require multistage reactor systems.[4–6]

Hydrogen is primarily used in proton-exchange membrane fuel cells (PEMFCs), which are sensitive to impurities. Contaminated hydrogen can severely degrade PEMFC performance, leading to lower efficiency and a shorter operational lifespan.[7] Therefore, there is a growing need for emission-free hydrogen-production methods that deliver high-purity hydrogen without the drawbacks associated with conventional processes. Catalytic methane decomposition (CMD), which is a single-stage process that produces hydrogen and solid carbon nanomaterials without CO_x emissions, is an emerging alternative to traditional hydrogen-production methods.[8] CMD is gaining significant attention because of its ability to generate turquoise hydrogen, a term used to describe hydrogen produced

Department of Applied Chemistry and Biochemical Engineering, Graduate School of Engineering, Shizuoka University, 3-5-1 Johoku, Chuo-ku, Hamamatsu, Shizuoka 432-8561, Japan. E-mail: watanabe.ryo@shizuoka.ac.jp

† Electronic supplementary information (ESI) available. See DOI: https://doi.org/10.1039/d5su00216h

from methane with minimal environmental impact. Turquoise hydrogen serves as a clean energy source for fuel cells, nuclear reactors, and industrial processes, whereas the co-produced nanocarbon can be used in electrodes, construction materials, batteries, and catalysts.[9]

CMD success depends on the reaction conditions and the catalyst used. Transition metals, such as nickel, iron, and cobalt, have shown high methane-decomposition activities owing to their abilities to effectively dissociate methane molecules.[10] Evenly distributed active sites are achieved when supported by high-surface-area materials, leading to high methane conversion rates and significant hydrogen yields. Recent studies have explored the addition of secondary metals, such as copper and zinc, to enhance efficiency and stability.[11] Nickel has demonstrated exceptional CMD potential owing to its high catalytic activity and stability. Studies have highlighted the effectiveness of Ni-nanoparticle-supported catalysts for delivering high methane-conversion rates and carbon solubility.[12,13] However, a major limitation of a Ni-based catalyst is its susceptibility to rapid deactivation due to carbon deposition and sintering at high operating temperatures.[12] To address these challenges, researchers have focused on bimetallic catalysts, which combine Ni with other metals, to improve their performance and durability.[14] Among secondary metals, Cu has emerged as a promising additive for Ni-based catalysts. Although Cu is less active toward methane decomposition owing to its filled d-band, it plays a critical role in enhancing the performance of a bimetallic Ni–Cu catalyst. Copper reportedly cleans active surfaces and prevents the catalyst from being encapsulated by carbon, thereby improving catalytic activity and longevity.[15] Sueleves *et al.* and others have demonstrated that the Cu in a Ni–Cu catalyst enhances methane adsorption and dissociation owing to the dilution effect, leading to higher conversion rates.[16] Additionally, Trevuera *et al.* showed that alloying Ni with Cu alters the Fermi energy level and modifies the d-band structure, which further improves catalytic performance.[17]

Despite their advantages, porous bimetallic Ni–Cu catalysts face challenges that hinder their CMD performance. The deposition of carbon, which covers active sites and reduces catalytic activity over time, is a major issue.[18] High operating temperatures also lead to metal sintering that causes metal particles to aggregate, resulting in a loss of active surface area.[19] Achieving a homogeneous distribution of active metals within the porous matrix is another challenge, as an uneven distribution can negatively affect the efficiency and stability of the catalyst.[20] Furthermore, excessive carbon deposition can lead to blocked pores that obstruct methane-diffusion pathways, and disrupt feed flow. These challenges highlight the need for advanced catalyst systems that are capable of maintaining consistent performance while mitigating carbon accumulation and pore blockage.

We used a hollow-wall-structured catalyst strategy to address the abovementioned issues. The single channel within the hollow-structured catalyst effectively mitigates carbon-induced feed-gas flow blockages. Additionally, their superior heat-transfer properties facilitate the rapid delivery of thermal energy to a catalyst plated on its surface, which is required for an endothermic reaction.[21] The carbon by-product can grow into the hollow spaces of the wall-structured catalyst, which is highly beneficial for carbon-capture applications.

We used electroless Ni and Cu plating to prepare catalysts. This technique is based on the difference in the electrode potentials of metal substrates and offers a versatile and efficient way of depositing a uniform layer of an active metal onto a substrate. This method facilitates precise control over the thickness and composition of the catalyst layer, thereby ensuring a high surface area and uniformly distributed active sites. It is particularly advantageous for creating complex geometries and structured catalysts because it enables intricate surfaces suitable for applications that require enhanced mass- and heat-transfer properties to be conformally coated. Studies have highlighted the wear resistance and durability of metal particles prepared using the electroless-plating (ELP) method.[22,23] Various preparation bases have been explored in studies on Ni/Al_2O_3 catalysts for decomposing methane, which revealed that particle morphology depends on the reducing agent.[24] However, to the best of our knowledge, new findings related to the performance of electroless-plated Ni–Cu catalysts have not been reported.

In this study, we focused on the use of electroless plating to synthesise a structured catalyst that simultaneously produces hydrogen and generates high-quality nanocarbon materials *via* CMD. The performance of the catalyst was evaluated under various operating conditions, with key parameters, such as temperature, promoter effects, and catalyst composition, comprehensively investigated to assess catalytic efficiency and stability. Our research examined the structural, morphological, and catalytic properties of a structured electroless-plated-catalyst in detail, with a focus on optimising its design for enhanced activity, selectivity, and resistance to deactivation. This multifaceted approach aimed to advance our understanding of structured catalysts for use in CMD and their potential for producing sustainable hydrogen and nanocarbon.

2 Experimental

2.1 Catalyst preparation

Four stainless steel (SLS) hollow-wall-type substrates (thickness: 4 × 2 mm; length: 25 mm; diameter: 20 mm diameter; density: 34 g cm^{-2}; apparent surface area: 14.1 cm^2) were used as hollow-wall substrates. Each substrate was first cleaned using 1 M aqueous NaOH solution and then activated in 50% HCl. An aluminium-triisopropoxide sol ($Al[OCH(CH_3)_2]_3$, 12 g; HNO_3 aq., 6 mL; HCHO, 4 mL; H_2O, 80 mL) was evenly applied to the inner surface of the substrate. The SLS hollow-wall substrate was then calcined at 800 °C (ramping time: 1.0 h; holding time: 2.0 h) to create a γ-alumina layer on its surface.

Alternating Pd–Sn plating was used to deposit Pd nuclei. The SLS hollow-wall-structural catalyst was immersed 20-times in the activation liquid ($PdCl_2$, 1.4×10^{-3} mol L^{-1}; HCl aq., 5.7×10^{-3} mol L^{-1}) and the sensitisation liquid ($SnCl_2 \cdot 2H_2O$, 1.1×10^{-3} mol L^{-1}; HCl aq., 5.7×10^{-3} mol L^{-1}). The formed nuclei were reduced using 3 M hydrazine. The substrate was then immersed in a nickel plating bath to deposit the nickel

component on its surface. Plating was performed for 30 min at 55 °C. The resulting catalyst was washed in a water bath and air-dried at room temperature.

Additional copper plating was performed by immersing the plate in a copper-plating solution and chemically reducing the deposited copper component on the surface. After cleaning in a water bath, the plate was dried in a humidity chamber for approximately 48 h to afford the SLS hollow-structured Ni–Cu based catalyst (Fig. 1).

2.2 Evaluating catalyst performance

Catalyst performance was examined using a fixed-bed reactor at a pressure 0.1 MPa by strictly adhering to the laboratory safety regulations of Japan. A normal-flow reactor was used in this study. The reactant gas was introduced into the reactor after the catalyst had been reduced at 600 °C for 1 h under a stream of hydrogen (44 mL min^{-1}). The methane flow rate was maintained at 50 mol min^{-1}. Methane was decomposed in the 500–800 °C temperature range in 50 °C increments, with each temperature held for 1 h. Nitrogen gas was fluxed into the reactor as the temperature was elevated, and methane was reintroduced upon stabilisation. The effluent gas from the reactor was analysed by gas chromatography (GC-8A; Shimadzu) with a thermal conductivity detector (TCD). Methane conversion (X_{CH_4}) was calculated using eqn (1), hydrogen production ($H_{2\ Production}$) was calculated using eqn (2), and the carbon-capture rate (CCR) was calculated at the end of the reaction and the total captured carbon had been collected using eqn (3).

$$\text{Conv. } (X_{CH_4}) = \frac{F_{CH_{4_{inlet}}} - F_{CH_{4_{outlet}}}}{F_{CH_{4_{inlet}}}} \times 100\% \quad (1)$$

$$H_{2\ Production} = \frac{H_{2_{outlet}}}{\text{time} \times \text{cat. weight}} \times 100\% \quad (2)$$

$$CCR(\%) = \frac{\text{Mass of carbon(g)}}{F_{CH_4}(\text{mol min}^{-1}) \times \text{time(min)} \times 12(\text{mol g}^{-1})} \times 100\% \quad (3)$$

2.3 Catalyst characterisation

The surface morphologies and cross-sections of the plated layers were investigated using field-emission scanning electron microscopy (FE-SEM, JEOL, JSM-7001F), and the elemental profiles of the same regions were evaluated using energy-dispersive X-ray spectroscopy (EDX, AMETEK, Pegasus). The layer-by-layer structure, and the fresh and alloy formations of each reduced catalyst were examined by X-ray diffractometry (XRD), Bruker Ultima (d-Tex/ultra) in the 10–90° 2θ range at 2° min^{-1} to confirm the SEM observations and SEM-EDX-determined particle-distributions. Additionally, the catalyst that exhibited optimal catalytic performance was subjected to *in situ* XRD using the same instrument to analyse the formation of alloy structures under reduction conditions (3-Flex, Micromeritics) using liquid nitrogen. The quantity of deposited Ni–Cu was determined by X-ray fluorescence (XRF, Supermini200, Rigaku, Inc.) spectroscopy. Additionally, the crystalline structures of the catalyst before and after reaction were examined by XRD (Ultima IV, Rigaku, Inc.) with Cu Kα radiation ($\lambda = 1.54$ Å). The structural properties of deposited carbon were characterized using micro-Raman spectroscopy (inVia Confocal Raman Microscope, Renishaw plc, UK) with a 532 nm excitation laser at 5 mW power.

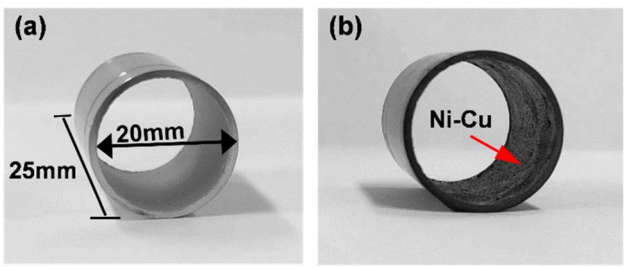

Fig. 1 Overview of the stainless-steel hollow-wall-type catalyst. (a) Before and (b) after electroless plating.

3 Results and discussion

3.1 Catalyst characterisation

The structures and compositions of the bimetallic Ni–Cu catalysts at various Cu loadings were investigated using FE-SEM. The fresh catalyst surface underwent significant morphological and chemical transformations upon reduction. Fig. 3(a) shows the fresh surfaces of various Cu-containing catalysts. Layered Cu-on-Ni surfaces were observed. The Ni in the as-prepared catalyst was notably poorly distributed, as shown in Fig. S1.† Cu clearly completely covered the active surface of the Ni that was exposed to the surface of the alloy structure upon reduction. Similarly, FE-SEM clearly showed a surface

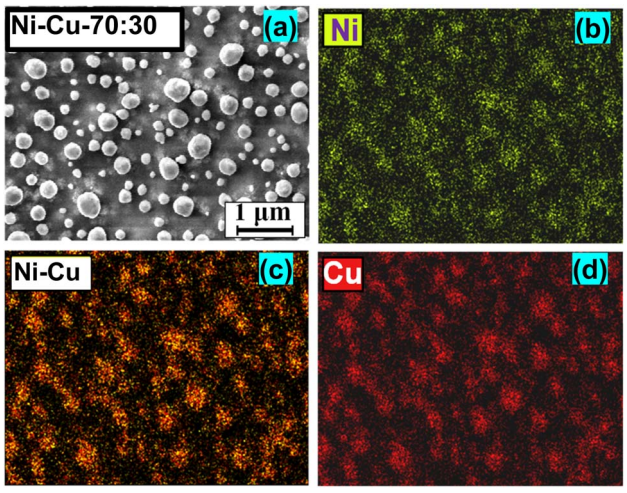

Fig. 2 (a) FE-SEM image of the reduced 70–30 catalyst, (b) SEM EDX analysis showing the elemental distribution of nickel, (c) SEM-EDX showing Ni and Cu distributions individually and under overlap conditions. (d) SEM-EDX showing the elemental distribution of the copper.

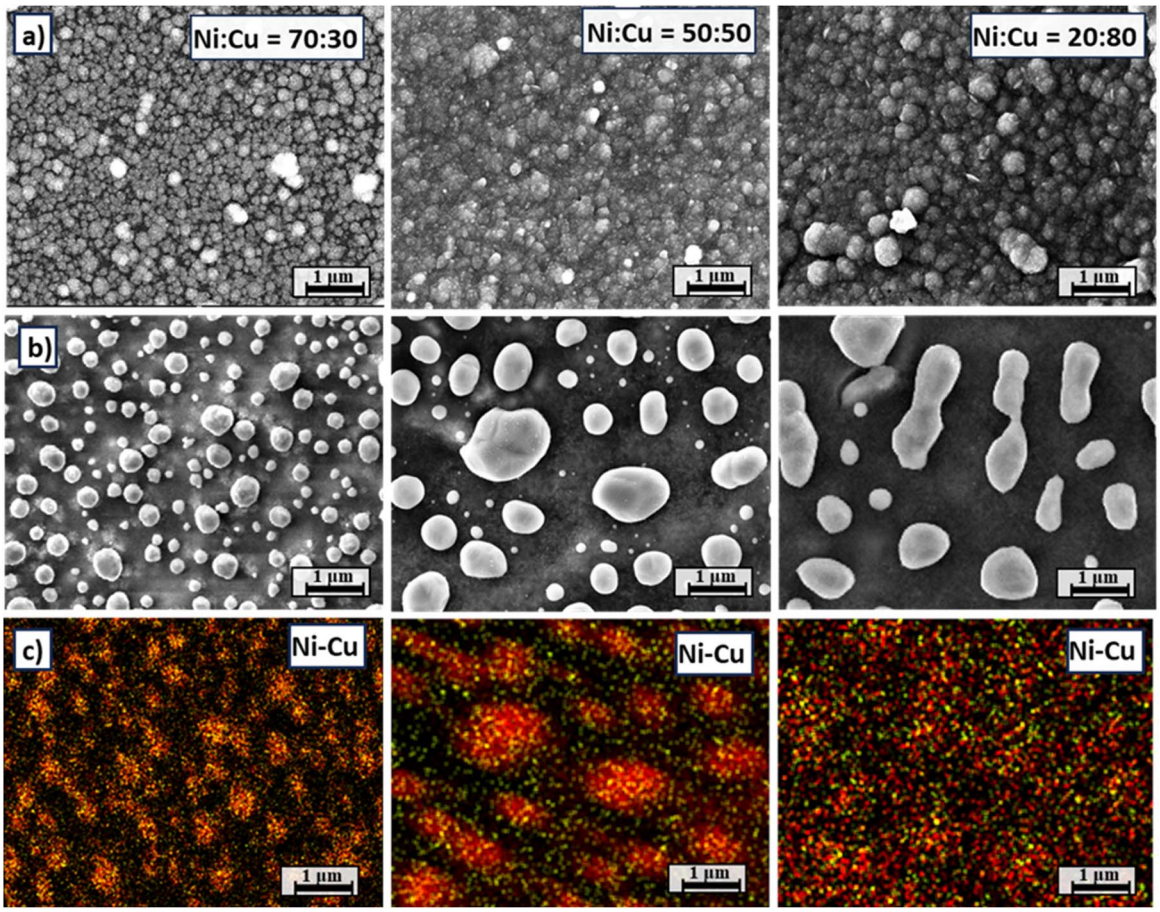

Fig. 3 (a) FE-SEM images of as-prepared catalyst samples. (b) FE-SEM images of reduced catalyst samples. (c) Overlapping SEM-EDX images showing Ni and Cu distributions.

morphology in which densely dispersed Cu predominantly increasingly occupies the surface of the alloy with increasing plating time during catalyst preparation. Hydrogen reduction led to the catalyst undergoing structural reorganisation and the formation of a separate alloy-island structure. The layer-by-layer arrangement of Ni and Cu in the fresh catalyst and the existence of the alloy structure were confirmed by XRD (Fig. S3†). The sizes of these alloy particles are strongly influenced by the Cu content. A higher Cu content led to the formation of larger Ni–Cu alloy islands, which is attributable to the lower reducibility and higher mobility of Cu that promotes diffusion and nucleation.[25] This phenomenon is clearly illustrated in Fig. 2 and 3(b), where changes in the corresponding Ni–Cu distribution are clearly evident during hydrogen reduction.

The overlapping SEM-EDX images in Fig. 2 and 3(c) show how the Ni and Cu are distributed. A lower Cu content results in smaller, more discrete Ni–Cu alloy particles with concentrated Ni and Cu distributions over the alloy structure. The Ni within the alloy matrix becomes more dispersed as the Cu content of the catalyst is increased. The active Ni content was found to be suppressed under bulk Cu nuclei resulting in dissipated Ni and Cu distributions. These findings highlight the role played by the Cu in modulating the structural and catalytic properties of the bimetallic Ni–Cu catalyst. The interplay between Cu reducibility, mobility, and its influence on Ni distribution is particularly valuable when designing and optimising further bimetallic catalysts for targeted applications.

Naghash *et al.* reported that a small amount of added copper helps to create carbon nanofibres and improves the life of the nickel-based catalyst by slowing deactivation. However, adding too much copper reduces the number of available active sites for decomposing methane, which lowers the overall conversion rate.[26] Similarly, Ermakova *et al.* reported that the addition of Cu (as a promoter) to a silica-supported Ni catalyst that contains more than 80% Ni enhances catalytic efficiency.[27] The alignment of our data with those mentioned above highlights the role played by Cu in modulating the structural and catalytic properties of a bimetallic Ni–Cu catalyst. This interaction, which is ascribable to the reducibility, mobility, and influence of Cu on the Ni distribution, is believed to be valuable when designing and optimising future bimetallic Ni–Cu catalysts for targeted applications.

3.2 Effect of copper as a promoter

Cu, as a promoter, provides one of the more cost-effective options for creating heterogeneous Ni–Cu catalysts. Studies have shown the carbon-diffusing effect of copper, which

indicates that it is not directly involved in catalysis.[28,29] The effect of temperature on the performance of individual metals during methane decomposition was examined using only copper- and nickel-plated samples, the results of which are shown in Fig. S4.† Nickel exhibited moderate catalytic activity, whereas copper showed no decomposition activity up to 700 °C; however a small amount of hydrogen was detected by GC as the temperature was increased to 750 and 800 °C. Decomposition was observed not to occur over the surface of the catalyst, but rather on the outer regions of the hollow stainless-steel substrate, which reveals that the observed decomposition activity is not directly due to the involvement of the copper in the catalyst, but rather to the thermal influence of the catalyst. No carbon capture was observed in the copper-only samples.

In contrast, nickel exhibited some catalytic activity, which increases slightly as the temperature was raised to 750 °C, with similar performance maintained as the temperature was increased to 800 °C, which highlights the high heat resistance of the Ni catalyst prepared by ELP. Catalytic activity significantly improved when Cu was introduced into the system. The performance of the best catalyst with respect to plating was compared with the performance of the Ni catalyst. The Ni catalyst with a moderate copper content exhibited overall improved performance at each temperature point as shown in Fig. 4.

A maximum promotion of 40% was observed at 750 °C, which is the temperature at which high conversion is typically observed. Hydrogen production per gram of catalyst per hour exhibited steady growth at each temperature. Copper lacks the necessary d-orbitals to effectively adsorb CH_4 molecules, rendering it inactive for methane decomposition. Nickel, on the other hand, possesses partially filled d-orbitals that facilitate methane adsorption and activation. However, the active sites on the Ni can become covered with filamentous carbon that grows during the decomposition process, which initially prolongs the decomposition process but eventually leads to catalyst deactivation due to encapsulation.

The introduction of Cu into the Ni catalyst system led to the formation of a Ni–Cu alloy that enhances the availability of active Ni sites. This alloying not only promotes catalytic activity but also helps to preserve active sites by preventing diffusion and encapsulation. Consequently, the Ni–Cu catalytic system exhibited significantly improved catalytic performance compared to that of Ni alone.

3.3 Effect of copper loading on catalytic activity

The net weight of the nickel in the SLS hollow-wall structure was approximately 0.03 g, and was deposited under standard ELP conditions on the internal surface of the hollow substrate, which has an area of 56 cm^2. The weight of Cu was varied by changing the plating time to produce a quartile range of Ni–Cu distributions. We initially focused on a 30-min copper-plating time for copper, at this point, a significant amount of Cu had been deposited.

The rate of copper deposition is expected to influence physicochemical factors, although this relationship is not yet fully understood. We observed a 50 : 50 Ni : Cu distribution after a 15-minute plating time. Additionally, we achieved an upper quartile distribution of 69 : 31 Ni : Cu after 7 minutes of copper plating, which we refer to as "70–30 Ni–Cu." For samples with higher copper content, we extended the copper plating time over the nickel surface to approximately 30 minutes or more. During the 30-minute plating process, intermediate Ni–Cu ratios were also obtained, which demonstrated similar performance, thereby highlighting the reproducibility of the results as shown in Fig. S5.† Among the various evaluated samples, 70–30 Ni–Cu exhibited excellent performance. Performance was observed to gradually decrease with increasing Cu concentration. Detailed plating data are provided in Table S1.†

Among the investigated samples, 20–80 Ni–Cu exhibited the worst performance up to 700 °C; however, anomalous improvements in catalytic performance were observed as the temperature was increased to 750 and 800 °C as shown in Fig. 5. The use of a higher amount of copper leads to coverage of the Ni active sites owing to nucleation during reduction. The XRD pattern of the fresh catalyst reveals the presence of metallic copper with increasing concentration (Fig. S6†) leading to lower activity owing to fewer available active sites.

All ELP-derived Ni–Cu catalysts exhibited progressively increasing performance with increasing temperature. Unlike porous catalysts, these catalysts are capable of withstanding

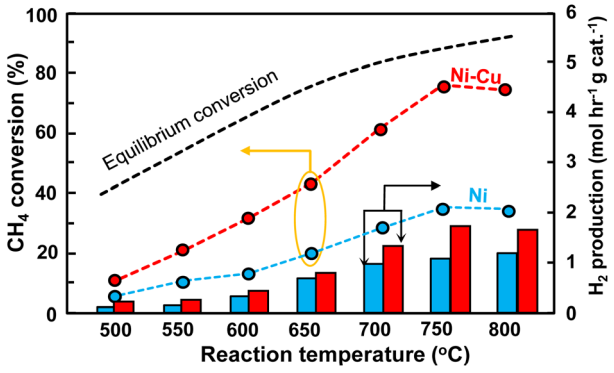

Fig. 4 Methane-conversion and hydrogen-production over Ni and Ni–Cu hollow-wall-structured catalysts prepared by ELP.

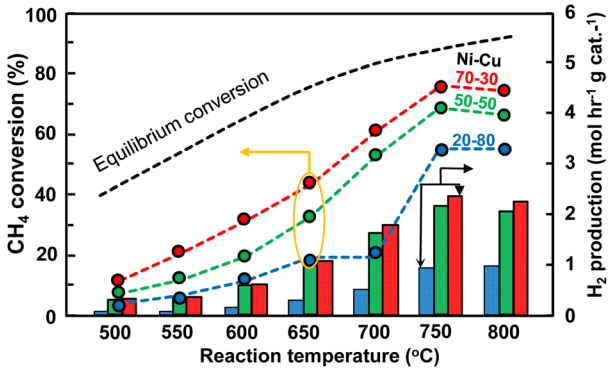

Fig. 5 Methane conversions and hydrogen productions over Ni–Cu catalysts with different Ni : Cu ratios.

elevated temperatures, even ones higher than those reported in the literature, with activity sustained to 800 °C, which highlights the high heat-resistance performance of these ELP-derived catalysts. These improvements are due to the nucleation of the Pd used for Ni deposition in the ELP method. Kawasaki *et al.* reported a similar tendency, where the combined influence of Pd and Ni resulted in highly heat-resistant alumina and silica supports.[24] The performance observed at various Ni : Cu ratios in our study is consistent with the findings of Wang *et al.*[30] Although our study delivered a higher maximum performance, it also used a catalyst weight of around 80 mg, which was almost half that of the Ni–Cu oxalate-based catalyst reported by Hang *et al.* Additionally, the heat resistance observed in our experiment is exceptional compared to that of the oxalate-based catalyst reported by Hang *et al.*

3.4 Effect of pre-treatment conditions on catalytic activity

Copper did not exhibit any significant catalytic activity. The metal in the as-prepared catalyst was distributed in a layered structure, with Cu deposited over Ni, consistent with the standard electrode potential series, in which Cu has a lower reduction potential than Ni. Cu has a high tendency to gain electrons and become deposited on the Ni surface, which is a prerequisite for the formation of the desired Ni–Cu alloy. Experiments were conducted using both as-prepared and reduced catalysts, with temperature maintained at 600 °C during reduction to ensure sufficient atomic Ni and Cu mobility to enable them to diffuse and form a homogeneous Ni–Cu alloy. This comparative study revealed that the pre-treatment conditions significantly influence catalytic activity.

The best-performing catalyst was evaluated under identical plating conditions in the presence and absence of pre-treatment. Because the metals were deposited *via* electroless plating, which involves layer-by-layer deposition, the absence of pre-treatment is detrimental to performance. Although methane-decomposition activity was observed for the non-pre-treated catalyst, the hydrogen yield was notably low, which is possibly ascribable to a self-reduction mechanism driven by consecutive methane decomposition, in which the hydrogen generated in this process is consumed to reduce the metal species. Pre-treatment was found to significantly enhance hydrogen production, with the optimal pre-treatment conditions leading to superior CH_4 conversion and high yields of hydrogen. The well-formed Ni–Cu alloy exhibited superior thermal stability and catalytic performance, whereas the as-prepared catalyst produced less hydrogen owing to inadequate alloying and incomplete metal reduction. Additionally, Cu flakes were observed over the deposited carbon, which is attributable to the reaction temperature inducing partial Cu mobility, which exposes active Ni sites that facilitate methane decomposition, whereas Cu, which is unable to form a composite structure with the active Ni particles, became isolated. This isolation led to flaking and lower hydrogen production, as not all Ni sites were available for catalysis. Consequently, the ELP Ni–Cu without pretreatment exhibited inferior initial catalytic performance compared to the pre-treated one as shown in Fig. 6.

3.5 Effect of plating-solution concentration

The amount of nickel loaded onto the catalyst was investigated. The normal loadings of Ni and Cu used in the ELP method are quite low (as low as 30 mg). Considering the low loading issue, we investigated increasing the concentration of the Ni–Cu catalyst by adjusting the concentration of the plating solution. We selected the best performing 70–30 Ni–Cu catalyst and examined the effect of the loading conditions. We increased the Ni concentration while maintaining a constant Cu content, and then examined the effect of increasing the concentrations of both Ni and Cu in the optimised catalyst.

Increasing the plating weight of the catalyst did not effectively improve catalytic activity. Even though higher loadings of Ni and Cu were obtained, the Ni-loading weight almost doubled, resulting in 53 mg of Ni deposited over a surface area of 56 cm. However, unexpected performance was observed as shown in Fig. 7. Bulk Ni loading led to a decline in performance compared to the dependency results observed across the studied temperature range, even when lower catalytic activity was observed, which was unexpected. Increasing the concentration of Ni alone resulted in lower performance, and

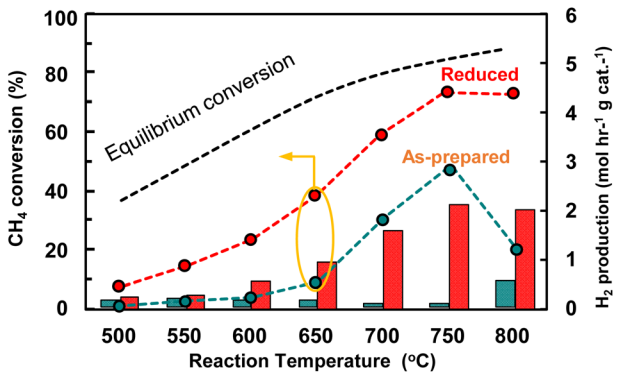

Fig. 6 Methane conversions and hydrogen productions over the optimised reduced and as-prepared Ni–Cu catalysts.

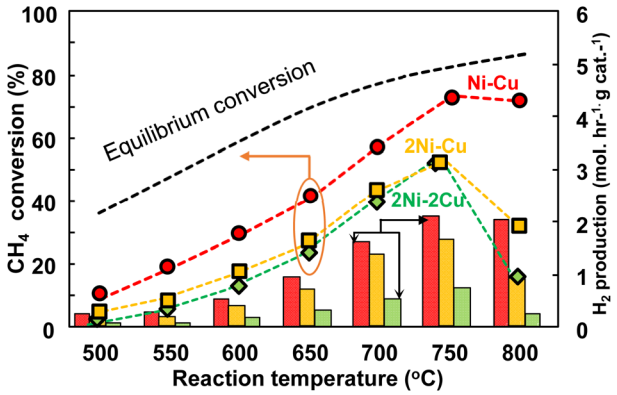

Fig. 7 Methane conversions and hydrogen production over the optimised Ni–Cu catalyst as the concentration of the Ni-plating bath was doubled.

increasing the Ni and Cu contents led to both catalysts losing their high-temperature-resistance characteristics. Bulk Ni and Cu particles were formed at higher concentrations (Fig. S7†), leading to Ni–Cu particles that were susceptible to sintering. The change in the Ni : Cu weight ratio is another factor responsible for the observed drop in performance. XRF analysis revealed that a doubly Ni-concentrated solution led to a 97 : 3 Ni : Cu ratio, while 92 : 8 was obtained when the concentrations of both plating solutions were increased.

Increasing the Ni concentration in the plating bath generally enhanced the deposition rate owing to the higher availability of Ni ions, as reported by Zhou *et al.*[31] Higher concentrations of Ni can lead to larger deposited particles, resulting in a rougher surface morphology. This bulking, which is observed at a higher plating-bath loading, can potentially affect catalytic activity. The Ni present in the alloy influences the crystallographic orientation and favours the (111) plane in FCC structures, which, along with smaller crystallites and less lattice strain, enhances hardness and bulkiness. Such bulk deposition and hardness are associated with a smaller surface area and fewer active sites that result in inferior catalytic activity, which can lead to slightly lower performance even when bulk copper is deposited. This reduction in active surface area eventually leads to lower catalytic activities at higher temperatures.

3.6 Effect of temperature on catalytic activity

Hydrogen reduction is a crucial step in the formation of catalytic alloys because it transforms metal oxides into their metallic forms, which is essential for alloy formation. Similarly, a suitable temperature promotes the diffusion of metal atoms to form a homogeneous metal-alloy mixture.[32] Tammann reduction temperature is considered to maintain structural integrity and agglomeration and sintering.[33] Such a reduction temperature is approximately 400 °C for copper, and 400–600 °C for nickel depending upon composition and particle size. Fig. 8 shows the 70–30 Ni–Cu catalyst at these three temperatures, which revealed that reduction at 400 °C exhibited the poorest catalytic performance. While the catalyst exhibited similar performance at 500 °and 600 °C, increasing the temperature to 800 °C led to a more significant performance drop. The best performance was observed at 600 °C.

The limited mobility of the Ni layer at lower temperatures is a contributing factor to its poor performance. Cu atoms are more mobile at 500 °C, resulting in more exposed surfaces and alloy formation. While initial conversions were comparatively lower than those observed at 600 °C, equivalent performance to that observed at 600 °C was achieved as the temperature was increased above 600 °C, which is possibly ascribable to sufficient energy leading to proper alloying and enhanced performance. Both Ni and Cu atoms are sufficiently mobile at 600 °C to properly diffuse and form a complete alloy structure, which is the expected reason for it exhibiting the best catalytic performance among the examined catalysts (Fig. 9).

We analysed the catalyst samples using *in situ* XRD to study structural differences and to further understand the observed performance drop. The XRD patterns of the fresh and reduced catalysts exhibited major (111) peaks, as shown in Fig. S5.† With this in mind, H_2 reduction was studied in detail with respect to this (111) peak.

H_2 reduction was investigated at various temperatures. Catalysts were first studied *via in situ* XRD with H_2 gas flowed at a feed rate of 25 mL h^{-1}. XRD patterns were obtained at different reduction temperatures, from room temperature to 700 °C, in 25 °C intervals to gain an understanding of minor and intermediate changes observed as the temperature is

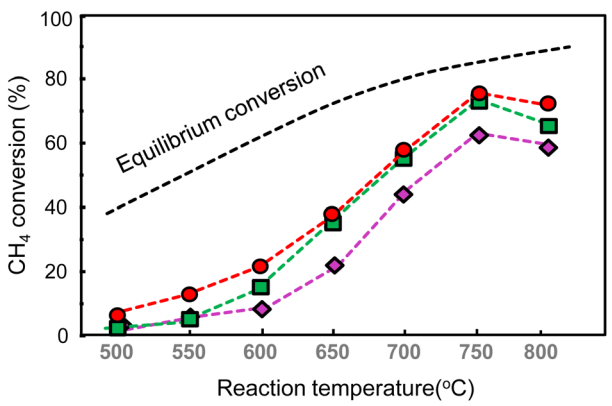

Fig. 8 Effect of reduction temperature on the methane-decomposition performance of the 70–30 Ni–Cu catalyst.

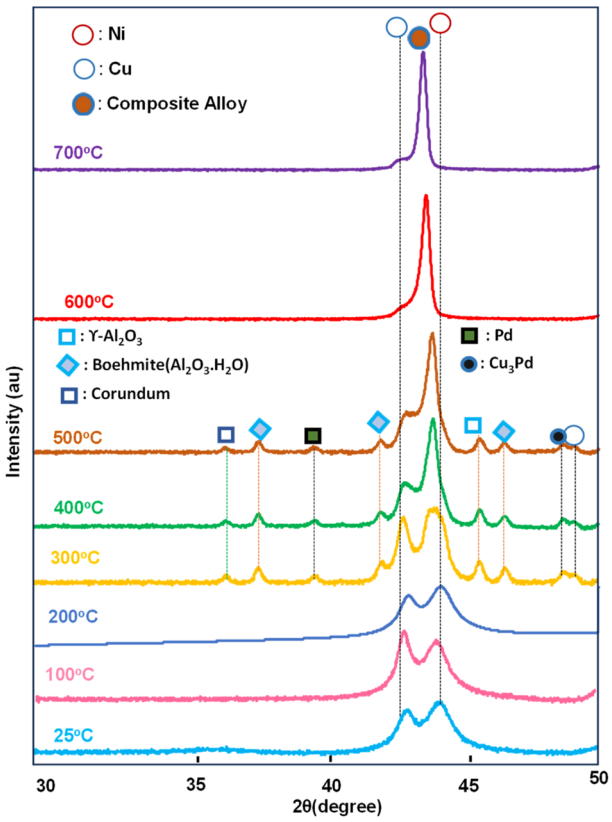

Fig. 9 Detailed *in situ* XRD profiles of 70–30 Ni–Cu acquired in the room-temperature to 700 °C range.

changed. XRD profiles acquired at major temperatures are shown in Fig. 8 and overall study in Fig S8†.

The catalyst exhibited no significant morphological changes during thermal treatment in the room-temperature to 700 °C range, as confirmed by structural and imaging analyses. A phase transformation was detected upon heating beyond 300 °C, which is primarily attributable to a transition in the aluminium oxide support phase, consistent with the thermal-stability limits of γ-alumina and its transformation into corundum and boehmite at elevated temperatures. Furthermore, palladium, which was used to promote adhesion during nickel deposition, became delocalised in the 300–580 °C temperature range, which is likely due to its high mobility and redistribution on the catalyst surface. The segregation of palladium away from the alloy is possibly the reason for the somewhat lower temperature drop observed for the 70–30 Ni–Cu catalyst reduced at 500 °C.

A well-defined and sharp alloying peak was observed at temperatures exceeding 600 °C, indicative of the formation of a stable bimetallic Ni–Cu phase. This alloying persisted up to 700 °C, albeit with a slight shift towards the Cu peak, which is possibly due to the high-temperature resurfacing of Cu particles away from the alloy structure. The formed composite alloy is the reason for the exceptional thermal stability and heat resistance of the bimetallic Ni–Cu catalyst prepared using ELP.

SEM-EDX imaging (Fig. S9†) revealed no significant degradation or agglomeration, thereby corroborating the structural integrity of the Ni–Cu alloy at high temperatures. This high thermal resistance is attributable to the unique fine-structured composite alloy of ELP-synthesised nanoparticles. Such composite structures may exhibit synergy through strong intermetallic bonding,[34] which facilitates the formation of smaller surface alloy domains, enhances their resistance to thermal sintering, and maintains structural stability under extreme conditions. Additionally, the strong metal–support interaction (SMSI) between the Ni and Cu alloy and the alumina substrate likely contributes to the observed thermal stability by preventing particle migration and coalescence. These findings reveal that the ELP-derived bimetallic Ni–Cu catalyst is a promising candidate for high-temperature catalytic applications, such as methane decomposition.

3.7 Comparing performance with that of conventional catalysts

A catalyst with the optimal composition was prepared using a conventional impregnation (IP) method, in order to comparatively evaluate the performance of the ELP catalyst. A stainless-steel substrate was coated with an aluminium oxide layer, and the wash-coat method was used to load the impregnation-based catalyst onto the surface. The IP-based Ni–Cu catalyst exhibited poorer performance under similar weight-loading and reduction conditions to that of the ELP-derived catalyst. Surface bulking during the reduction process is shown in the supplementary figure. The Ni–Cu catalyst exhibited negligible overall performance under the same weight conditions; indeed, high performance was not observed even when the weight was increased by a factor of 2.5.

Based on the SEM images, we attempted to increase the weight by a factor of five and then tested the durability of the catalyst. The IP-derived catalyst did not deliver the same performance as the ELP-derived catalyst despite this massive increase in weight. Under these weight-loading conditions, the IP catalyst exhibited significantly improved performance. Fig. 10 presents a comparative analysis of the catalytic performance between the ELP catalyst and IP catalyst, (5× weight). Both catalysts demonstrated enhanced activity with increasing temperature up to 750 °C. Notably, the ELP catalyst exhibited superior performance relative to the IP catalyst across this temperature range. At 800 °C, the ELP catalyst maintained stable activity, whereas the IP catalyst experienced complete deactivation. This highlights the thermal stability of the ELP catalyst under high-temperature conditions, despite its significantly lower metal loading.

The hydrogen production per gram of catalyst was determined to be 2.3 mol h^{-1} $g_{cat}{}^{-1}$, which is almost ten-times higher than that of the IP-based catalyst. The bulk surface morphology (Fig. S10†) of the IP-derived catalyst is believed to be the reason for its low number of active sites; consequently, such bulk structures are susceptible to sintering at high temperatures.

3.8 Characterising the carbon deposit

Carbon is a valuable by-product generated during catalytic methane decomposition (CMD), and the SLS hollow wall-structured catalyst exhibits good performance in terms of both carbon capture and the quality of the produced carbon. Carbon was uniformly deposited across the entire structured-catalyst substrate, from the inlet to the outlet (Fig. 11), indicative of consistent catalytic activity, and consisted of high-density carbon nanofibers with thin nanostructures of uniform size, which demonstrates the ability of the catalyst to produce high-quality carbon materials (Fig. 12 and 13).

Thin and fine precipitated carbon was consistently obtained even when the catalyst composition was varied, as shown in Fig. S12,† which highlights the potentially valuable carbon-capture application of the ELP-derived wall substrate. The carbon-capture rate was observed to decrease significantly with increasing Cu content. However, the nature of the captured

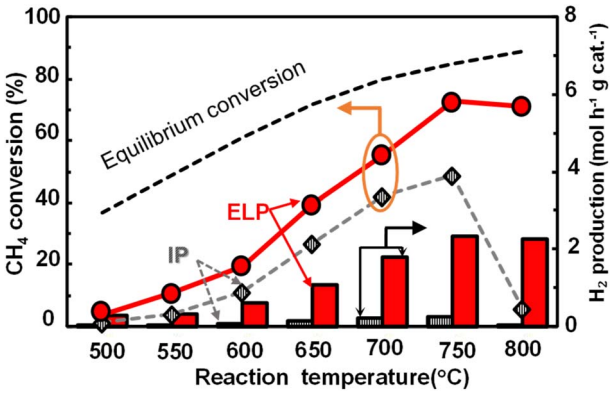

Fig. 10 Comparing the H_2 production and CH_4 conversion of the ELP- and IP-derived catalysts.

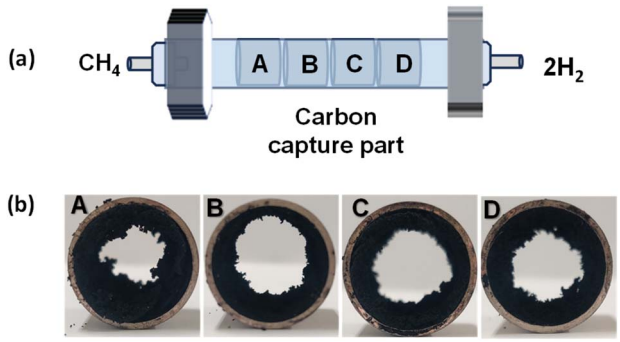

Fig. 11 (a) Schematic representation of the CMD setup and the structured catalyst position. (b) Images showing carbon capture by the ELP-derived 70–30 Ni–Cu catalyst.

carbon was consistent across all ELP-derived Ni–Cu catalysts (Fig. 12 and S12†). The 70–30 Ni–Cu catalyst captured the most carbon (36.6%), followed by 50–50 (32.2%), and the 20–80 catalyst (26.7%). We analysed the carbon tip using SEM-EDX to investigate such differences in carbon-capture performance, which revealed that this fraction of carbon precipitates followed a tip-growth mechanism.[35]

Elemental compositional analysis can help clarify the observed variations in the carbon-capture rate, as the catalyst containing a moderate amount of copper exhibited a slender carbon-growth mechanism in which filamentous carbon grows continuously from active alloy particles. However, a high Cu content resulted in improper carbon growth with metals found to be distributed throughout the carbon structures of the carbon nanotubes (CNTs). The CNTs were 20–80 nm in diameter. Interpreting the nature of the carbon in each carbon sample and anticipating its applicability is quite challenging based on its external morphological appearance; consequently, we examined each carbon sample by Raman spectroscopy.

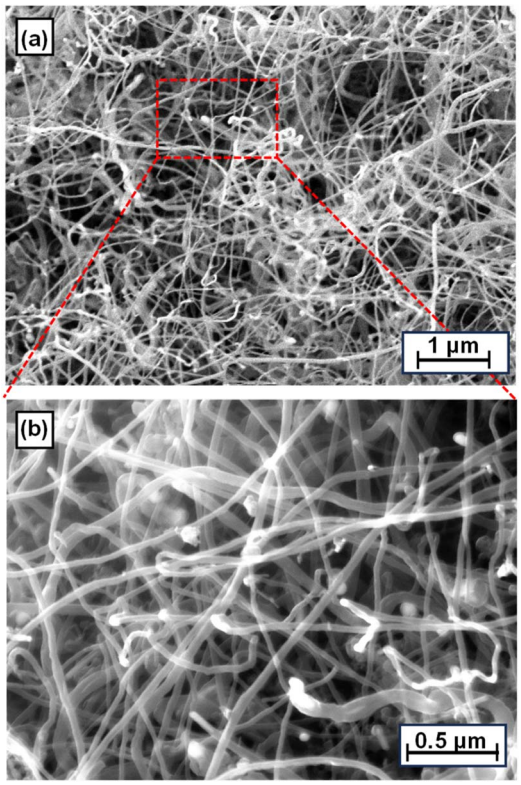

Fig. 12 FE-SEM carbon-capture images for the 70–30 catalyst at (a) 20 K and (b) 30 K magnification.

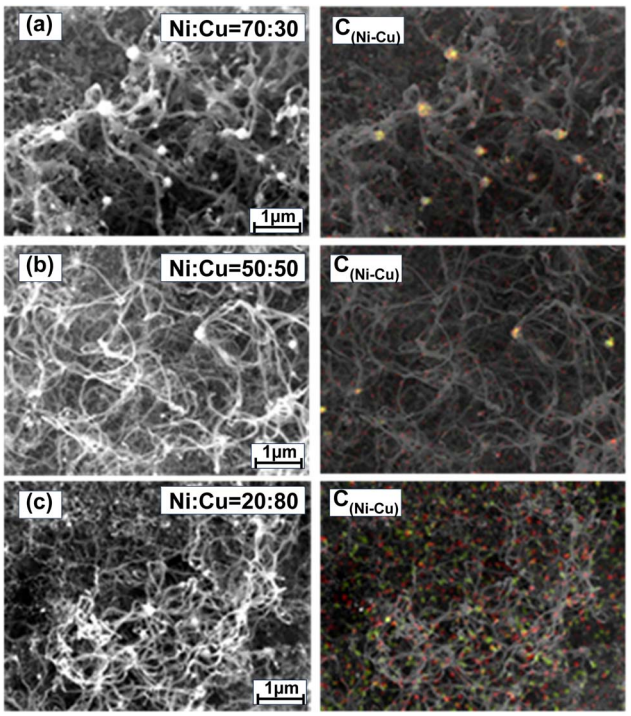

Fig. 13 Carbon elemental compositional analyses for the ELP-derived Ni–Cu catalysts after the reaction.

The I_D/I_G ratio, which is derived from the intensities of the D and G Raman bands, is a common metric used to assess the quality of a carbon material. A lower I_D/I_G ratio is suggestive of fewer defects and a higher degree of graphitisation, consistent with higher-quality carbon.[36] The Raman spectrum of a carbon material can be deconvoluted into several bands, including the G and D bands, and the degree of graphitisation, which is indicative of structural order, can be inferred from these spectra. A higher degree of graphitisation typically corresponds to fewer defects and a more ordered structure, and is considered to correspond to higher quality.[22] Deconvoluting Raman spectra can help separate the contributions of various bands. In particular, the width of the D-band correlates well with the degree of disorder, with a narrower D band suggestive of less disorder and a higher-quality carbon material, as a consequence, while a broader D-band is indicative of greater disorder.[22,36] The I_G/I_D ratios of the synthesised CNTs are plotted as functions of the process scenario in Fig. 14(a). Among the various samples, the nanocarbon derived from the 20–80 catalyst exhibited an I_G/I_D ratio greater than 0.6, indicative of a moderate level of structural defects. In contrast, the best performing catalyst exhibited an I_G/I_D ratio of 0.83, which is greater than that reported for commercial CNTs ($I_G/I_D = 0.74$).[37]

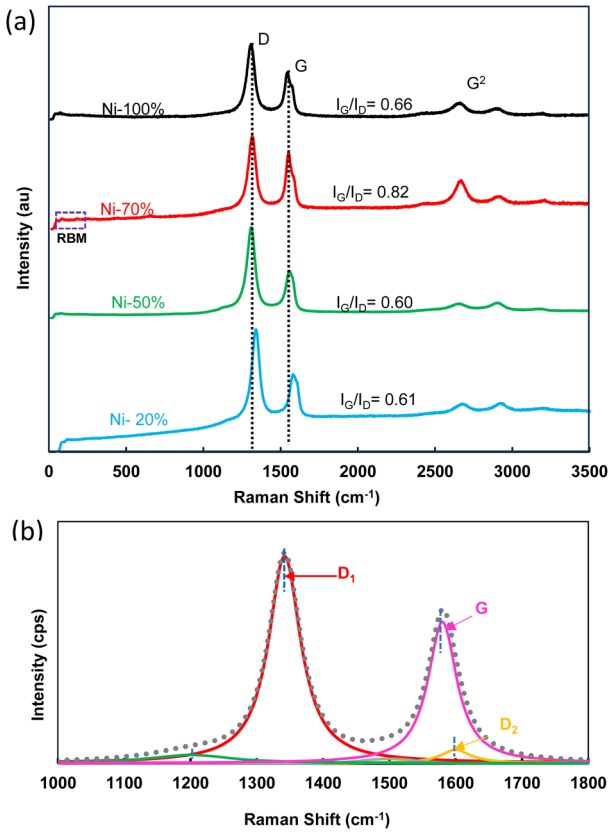

Fig. 14 (a) Comparative Raman spectra of carbon in the ELP catalyst with different Ni contents. (b) Deconvoluting the peaks in the spectrum of the 70–30 Ni–Cu catalyst.

In addition, the corresponding Raman spectrum shows a lower degree of D-band deconvolution, consistent with less sp^3-based disorder within the carbon, which suggests that the optimised catalyst produces CNTs with superior graphitic quality and fewer defects as shown in Fig. 14(b). Furthermore, a traceable radial-breathing-mode peak was observed in the Raman spectrum of the 70–30 Ni–Cu catalyst, whereas it was undetectable in the spectra of the other samples. This implies the presence of a small fraction of single-walled and double-walled CNTs in the 70–30 Ni–Cu sample, with the former dominating. The 70–30 Ni–Cu catalyst produced CNTs exhibiting an intense G^2 band (~2650–2700 cm^{-1}), a second-order overtone of the D band arising from a double-resonance process involving two phonons with opposite momentum.[38] The presence of three distinct subpeaks in the G^2 band as can be seen on Fig. 14(a) indicates bilayer-like stacking in the CNT walls, consistent with the splitting behaviour observed in few-layer graphene systems (where bilayer graphene typically shows three components). This well-resolved multiple structure, combined with the high G^2 band intensity, confirms superior graphitization and structural order in the synthesized CNTs, making them particularly suitable for electronic applications requiring defined crystallinity.

Carbon materials with moderate defect levels (as indicated by an I_G/I_D ratio of approximately 0.8) are particularly suitable for various electronic applications.[37] The Cu incorporated in the catalyst plays a critical role in promoting the formation of filamentous carbon with low structural disorder. This observation is consistent with previous studies, such as those of Nagash *et al.*, which highlighted the beneficial effects of Cu in enhancing carbon-nanostructure quality.[26] In our study, the ELP method ensured the formation of small catalyst particles, which facilitated the growth of filamentous carbon across all samples. However, slightly lower concentrations of Cu not only promoted filamentous carbon growth but also improved the overall CNT quality. This improvement is attributable to the cleaning effect of Cu, which enhances the availability of active sites and optimises carbon diffusion through the alloy structure. In contrast, catalysts with higher Cu contents exhibit more-dispersed Ni and Cu distributions that may hinder carbon diffusion and lead to the formation of less-ordered carbon structures. This phenomenon is likely ascribable to the lower availability of active sites and altered carbon-diffusion pathways in the bulk Cu-rich catalysts.

4 Conclusions

The Ni–Cu catalyst synthesized *via* electroless plating (ELP) formed finely layered structures that alloyed uniformly upon reduction. Cu incorporation enhanced catalytic performance over monometallic Ni by improving metal dispersion and active-site modification, but excessive Cu loading caused nanoparticle agglomeration, reducing activity. Reduction at 600 °C promoted stable Ni–Cu alloying, with Ni diffusing with Cu layers. ELP-derived catalysts outperformed impregnation-prepared ones in methane decomposition and hydrogen production. The 70–30 Ni–Cu ratio achieved optimal performance, yielding highly graphitized carbon nanotubes (CNTs) ($I_G/I_D = 0.83$), superior to commercial CNTs. These CNTs, with moderate defect density, are suitable for electronics and nanomaterials. Cu facilitated filamentous carbon growth and improved CNT quality *via* surface cleaning and active-site accessibility. The results demonstrate ELP's advantage in producing thermally stable, efficient bimetallic catalysts. The 70–30 Ni–Cu catalyst shows promise for turquoise hydrogen and carbon capture application with further optimization potential in metal distribution and loading.

Data availability

The data that support the findings of this study are available from the corresponding author, Ryo Watanabe, upon reasonable request.

Conflicts of interest

There are no conflicts to declare.

Acknowledgements

This work is supported by JST-ALCA-Next Program Grant Number JPMJAN24C2, Japan.

References

1 S. Kumar and K. Rathore, *Int. J. Mater. Manuf. Sustain. Technol.*, 2023, **2**, 1–15.
2 S. E. Hosseini and M. A. Wahid, *Renewable Sustainable Energy Rev.*, 2016, **57**, 850–866.
3 M. N. Uddin, V. V. Nageshkar and R. Asmatulu, *Energy, Ecol. Environ.*, 2020, **5**, 108–117.
4 T. J. Crowley, *Science*, 2000, **289**, 270–277.
5 R. M. Navarro, M. A. Pena and J. L. G. Fierro, *Chem. Rev.*, 2007, **107**, 3952–3991.
6 S. Takenaka, *Res. Chem. Intermed.*, 2006, **32**, 263–278.
7 B. C. Steele and A. Heinzel, *Nature*, 2001, **414**, 345–352.
8 X. Liu, X. Wang and H. Li, *Int. J. Hydrogen Energy*, 2023, **48**, 3104–3117.
9 Y. Zhang and L. Liu, *J. Mater. Sci. Technol.*, 2022, **72**, 139–146.
10 T. A. Nguyen and J. Park, *Catal. Sci. Technol.*, 2021, **11**, 2274–2289.
11 D. Wang and Y. Chen, *J. Catal.*, 2021, **392**, 100–108.
12 H. Zhang and L. Xu, *J. Catal.*, 2020, **381**, 15–23.
13 Z. Chen and X. Wu, *Catal. Today*, 2020, **350**, 79–86.
14 A. M. Amin, E. Croiset and W. Epling, *Int. J. Hydrogen Energy*, 2011, **36**, 2904–2935.
15 S. E. Shoemaker, S. Bismeijer, D. F. Wezendonk, J. D. Meeldijk, T. A. Welling and P. E. de Jongh, *Mater. Adv.*, 2024, **4**, 4251–4261.
16 J. M. Sueleves and M. Pérez-Periñán, *Catal. Lett.*, 2019, **149**, 2025–2032.
17 F. Trevuera, J. Rodríguez and P. Villota, *Appl. Catal., A*, 2018, **564**, 132–139.
18 F. Zhao and Z. Li, *Catal. Sci. Technol.*, 2021, **11**, 907–917.
19 R. Patel and A. Kumar, *J. Catal.*, 2020, **389**, 97–106.
20 H. Wang and X. Zhao, *Appl. Catal., A*, 2019, **570**, 51–59.
21 C. Fukuhara, R. Hyodo, K. Yamamoto, K. Masuda and R. Watanabe, *Appl. Catal., A*, 2013, **468**, 18–25.
22 K. N. Srinivasan, R. Meenakshi, A. Santhi, P. R. Thangavelu and S. John, *Surf. Eng.*, 2010, **26**, 153–158.
23 M. H. Staia, E. J. Castillo, E. S. Puchi, B. Lewis and H. E. Hintermann, *Surf. Coat. Technol.*, 1996, **86**, 598–602.
24 W. Kawasaki, H. Kato, R. Sakhon, R. Watanabe and C. Fukuhara, *J. CO_2 Util.*, 2017, **22**, 91–96.
25 A. C. Lua and H. Y. Wang, *Appl. Catal., B*, 2013, **132**, 469–478.
26 A. R. Naghash, Z. Xu and T. H. Etsell, *Chem. Mater.*, 2005, **17**, 815–821.
27 M. A. Ermakova, D. Y. Ermakov and G. G. Kuvshinov, *Appl. Catal., A*, 2000, **201**, 61–70.
28 W. Yang, Y. Feng and W. Chu, *J. Nanotechnol.*, 2014, **2014**, 547030.
29 D. Torres, J. L. Pinilla and I. Suelves, *Appl. Catal., A*, 2018, **559**, 10–19.
30 H. Y. Wang and A. C. Lua, *Chem. Eng. J.*, 2015, **262**, 1077–1089.
31 Q. Zhou, G. Li, Z. Zhou, Y. Qu, R. Chen, X. Gao and R. Li, *J. Alloys Compd.*, 2021, **863**, 158467.
32 S. M. Gericke, J. Rissler, M. Bermeo, H. Wallander, H. Karlsson, L. Kollberg and S. Blomberg, *Catalysts*, 2022, **12**, 755.
33 R. J. Farrauto, L. Dorazio and C. H. Bartholomew, *Introduction to catalysis and industrial catalytic processes*, John Wiley & Sons, 2016.
34 E. Ma and T. Zhu, *Mater. Today*, 2017, **20**, 323–331.
35 R. T. Yang and J. P. Chen, *J. Catal.*, 1989, **115**, 52–64.
36 C. Hu, S. Sedghi, A. Silvestre-Albero, G. G. Andersson, A. Sharma, P. Pendleton and M. J. Biggs, *Carbon*, 2015, **85**, 147–158.
37 R. Rattanaamonkulchai, T. Kludpantanapan, A. Srifa, W. Koo-Amornpattana, W. Chaiwat, C. Sakdaronnarong and S. Ratchahat, *J. Environ. Chem. Eng.*, 2022, **10**, 107910.
38 J. S. Park, A. Reina, R. Saito, J. Kong, G. Dresselhaus and M. S. Dresselhaus, G′ band Raman spectra of single, double and triple layer graphene, *Carbon*, 2009, **47**(5), 1303–1310.